Editors' Suggestion

Observation of Nonaxisymmetric Standard Magnetorotational Instability Induced by a Free-Shear Layer

Yin Wang,[1,*] Fatima Ebrahimi,[1,2] Hongke Lu,[3] Jeremy Goodman,[2] Erik P. Gilson,[1] and Hantao Ji[1,2]
[1]*Princeton Plasma Physics Laboratory, Princeton University, Princeton, New Jersey 08543, USA*
[2]*Department of Astrophysical Sciences, Princeton University, Princeton, New Jersey 08544, USA*
[3]*Thayer School of Engineering, Dartmouth College, Hanover, New Hampshire 03755, USA*

(Received 5 November 2024; accepted 18 February 2025; published 31 March 2025)

The standard magnetorotational instability (SMRI) with a magnetic field component parallel to the rotation axis is widely believed to be responsible for the fast accretion in astronomical disks. In conventional base flows with a Keplerian profile or an ideal Couette profile, most studies focus on axisymmetric SMRI, since excitation of nonaxisymmetric SMRI in such flows requires a magnetic Reynolds number (Rm) more than an order of magnitude larger. Here, we report that, in a magnetized Taylor-Couette flow, nonaxisymmetric SMRI with an azimuthal mode number $m = 1$ can be triggered by a free-shear layer in the base flow at $\mathrm{Rm} \gtrsim 1$, the same threshold as for axisymmetric SMRI. Global linear analysis reveals that the free-shear layer reduces the required Rm, possibly by introducing an extremum in the vorticity of the base flow. Nonlinear simulations validate the results from linear analysis and confirm that a novel instability recently discovered experimentally [Wang *et al.*, Nat. Commun. **13**, 4679 (2022)] is the nonaxisymmetric $m = 1$ SMRI. Our finding has astronomical implications as free-shear layers are ubiquitous in celestial systems, such as the disk-star boundary layer, the solar tachocline, and the edge of planet-opened gaps in protoplanetary disks.

DOI: 10.1103/PhysRevLett.134.135101

The magnetorotational instability (MRI), a linear magnetohydrodynamic (MHD) instability in a differentially rotating conductive flow with a magnetic field, is thought to be the main cause of turbulence that leads to outward transport of angular momentum and inflow of mass (accretion) in astronomical disks [1–5]. An MRI-active accretion disk consists of partially or fully ionized and magnetized plasma [6] orbiting a compact massive object such as a black hole or protostar. Outside of the innermost stable circular orbit, such flow has a Keplerian angular velocity profile $\Omega(r) \propto r^{-3/2}$, with r being the radial distance from the central object. Among astrophysically relevant variants of MRI, the "standard MRI" (SMRI) with an axial magnetic field [2–4] is of most interest, due to its theoretical simplicity and relative ease of experimentation compared to radial or toroidal magnetic fields. SMRI is insensitive to radial boundary conditions (BCs), which is particularly important for accretion disks as the radial boundaries are generally uncertain and uncontrolled. Given a finite magnetic diffusivity η and an appropriate length scale L, SMRI requires a magnetic Reynolds number $\mathrm{Rm} \equiv \Omega L^2/\eta \gtrsim 1$. It also requires a moderate magnetic field: $V_\mathrm{A} \lesssim \Omega L$, where $V_\mathrm{A} = B/\sqrt{\mu_0 \rho}$ is the Alfvén speed based on the field strength B, vacuum permeability μ_0, and mass density ρ. These characteristics distinguish SMRI from inductionless variants of MRI that persist in the zero-Rm limit provided that dimensionless numbers scaling with B^2/η remain nonzero (e.g., Elsässer number $\Lambda = V_\mathrm{A}^2/\eta\Omega$ or squared Hartmann number $\mathrm{Ha}^2 = V_\mathrm{A}^2 L^2/\eta\nu$) [7–10]. These inductionless variants require field strengths, field geometries, and shear profiles not characteristic of most accretion disks [11,12].

Although the Event Horizon Telescope has captured images of black-hole accretion disks that align with general relativistic MHD simulations [13,14], the presence of SMRI and other astrophysical instabilities cannot be directly confirmed through observation due to the telescope's limited resolution. MRI experiments are thus necessary, which often involve a swirling flow created in a Taylor-Couette device consisting of two coaxial cylinders that rotate independently to viscously drive the liquid metal between them. Ideally, such a flow has an ideal Couette rotation profile, $\Omega(r) = a + b/r^2$, with constants a and b determined by the rotation speeds of the two cylinders. According to Rayleigh's criterion [15], a quasi-Keplerian rotation profile with $0 < q = -(r/\Omega)\partial\Omega/\partial r < 2$ is linearly stable to hydrodynamic (non-MHD) axisymmetric perturbations. Experiments further indicate that when secondary flows due to end effects are minimized with independently rotating end caps, quasi-Keplerian hydrodynamic flows are nonlinearly stable as well [16]. With the addition of an axial magnetic field, SMRI has been demonstrated in a quasi-Keplerian liquid-metal flow [17]. Previous studies of SMRI mainly focused on its axisymmetric version. This is because,

*Contact author: ywang3@pppl.gov

although nonaxisymmetric SMRI is essential for astrophysical dynamos [18–25], it requires a higher Rm in ideal Couette flow out of reach of current experiments [26,27], perhaps except for the upcoming "DRESDYN-MRI" experiment [28–32]. On the other hand, the ideal Couette profile cannot be fully realized in an actual device with an axial magnetic field due to end effects, and a vertical free-shear layer [Stewartson-Shercliff layer [33–35] (SSL)] is formed, creating a local maximum in $q(r)$ [36,37]. While the stability of the SSL has been elucidated [38,39], its impact on SMRI, whether axisymmetric or nonaxisymmetric, has been less studied. Although constant in the idealized accretion disk discussed above, q likely varies with radius in actual celestial systems. This includes disk-star boundary layers [40,41], edges of planet-opened gaps [42,43], the solar tachocline [44,45], and perhaps due to radial entropy gradients [46].

Here, based on global linear analysis and nonlinear simulations of liquid-metal Taylor-Couette flows, we report for the first time that an SSL in a hydrodynamically stable axisymmetric base flow can introduce nonaxisymmetric SMRI at $\mathrm{Rm} \gtrsim 3$, a similar threshold for the axisymmetric SMRI. The nonaxisymmetric SMRI is an axial standing wave with an azimuthal mode number $m = 1$, which is the most unstable of the $m \geq 1$ modes. It leads to a global $m = 1$ radial magnetic field B_r in the midplane, which increases significantly with Rm consistent with the recent experimental observation [26]. Like $m = 0$ SMRI, the SSL-induced $m = 1$ SMRI also gives rise to an outward flux of axial angular momentum.

Experimental details are described elsewhere [26], and we only mention key points here (see Fig. 1). The working fluid is a GaInSn eutectic alloy (Galinstan) [67% Ga, 20.5% In, 12.5% Sn, $\rho = 6.36 \times 10^3$ kg/m^3, conductivity $\sigma_G = 3.1 \times 10^6$ $(\Omega m)^{-1}$], liquid at room temperature. The fluid-facing surfaces of the inner and outer cylinders have radii $r_1 = 7.06$ and $r_2 = 20.3$ cm and height $H = 28.0$ cm. The inner cylinder is composed of five insulating Delrin rings (green). The outer cylinder is made of stainless steel [gray; $\sigma_s = 1.45 \times 10^6$ $(\Omega m)^{-1}$]. Insulating radial BCs are thus suitable for the experiment, which do not require a zero radial magnetic field like conducting BCs (Supplemental Material [47]). The upper and lower copper [$\sigma_{Cu} = 6.0 \times 10^7$ $(\Omega m)^{-1}$] end caps are divided into two rings at $r_3 = 13.5$ cm. They provide inductive coupling to the fluid, enabling the nonlinear saturation of $m = 0$ SMRI to detectable levels [17,50,51]. The rotation speeds of the inner cylinder (Ω_1), upper (lower) inner ring (Ω_3), and upper (lower) ring (Ω_2) outer cylinder (Ω_2) have a fixed ratio $\Omega_1 : \Omega_2 : \Omega_3 = 1 : 0.19 : 0.58$, which, together with two 1-cm stainless steel flanges attached to the inner cylinder, help minimize the hydrodynamic Ekman circulation [52]. Six coils provide a uniform axial magnetic field $B_i \leq 4800$ G through the rotating liquid metal. Hall probes on the inner cylinder measure the local radial magnetic field $B_r(t)$ in the midplane ($z/H = 0.5$) at various azimuths. Dimensionless measures of the rotation and field strength are the magnetic Reynolds number $\mathrm{Rm} = r_1^2 \Omega_1 / \eta$ and the Lehnert number $B_0 = B_i / r_1 \Omega_1 \sqrt{\mu_0 \rho}$, which are varied in the ranges $\mathrm{Rm} \lesssim 4.5$ and $B_0 \lesssim 1.2$. Here ν and η are the kinematic viscosity and magnetic diffusivity of Galinstan, and the magnetic Prandtl number $\mathrm{Pr}_m = \nu/\eta = 1.2 \times 10^{-6}$. For each run, the device first spins up for 2 min. B_i is then imposed, and the flow relaxes into a statistically steady MHD state within 2 sec.

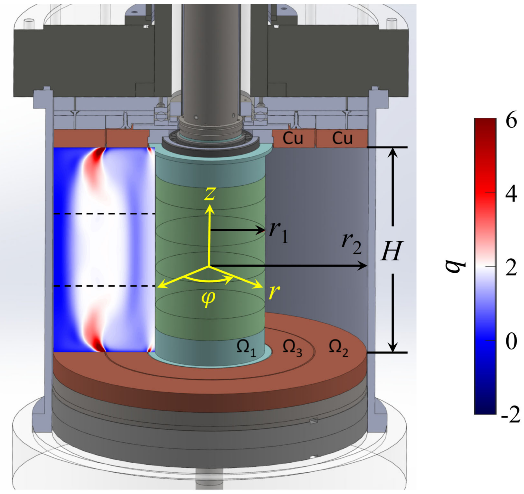

FIG. 1. Sketch of the Taylor-Couette cell used in the experiment. It has three independently rotatable components: the inner cylinder (Ω_1), outer-ring-bound outer cylinder (Ω_2), and upper (lower) inner rings (Ω_3). The contour plot shows the φ-averaged shear profile q, in the statistically steady MHD state at $\mathrm{Rm} = 4$ and $B_0 = 0.2$ from 3D simulation. The cylindrical coordinate system used is shown in yellow. The $\Omega(r)$ averaged between the two horizontal dashed lines is the base flow for calculating the growth rate of the $m = 1$ SMRI in Fig. 2.

Our simulations use the open-source code SFEMaNS to solve the Maxwell and Navier-Stokes equations for incompressible flows in a fluid-solid-vacuum domain similar to our experiments. Details on the code and mesh setup are available elsewhere [17,26,53]. The main limitation of our simulations is the Reynolds number, which is $\mathrm{Re} = r_1^2 \Omega_1 / \nu \sim 10^3$, compared to $\mathrm{Re} \sim 10^6$ in the experiment. We conducted two types of simulations: "3D" nonlinear simulations with $m = 0$–31 modes, run to the saturated MHD state for comparison with experimental results across a range of Rm and B_0 values; and "2D + 1" linear simulations that were first run to axisymmetric MHD saturation with an SSL ($m = 0$ only, $B_i > 0$), then activated $m = 1$ terms to simulate the exponential growth phase under realistic axial boundary conditions. For comparison, we also performed "1D" global linear analyses using the open-source code DEDALUS [54]. Since DEDALUS allows only one nonperiodic dimension, these calculations assume eigenmodes $\propto \exp[i(-\omega t + m\varphi + n\pi z/H)]$: i.e., periodic

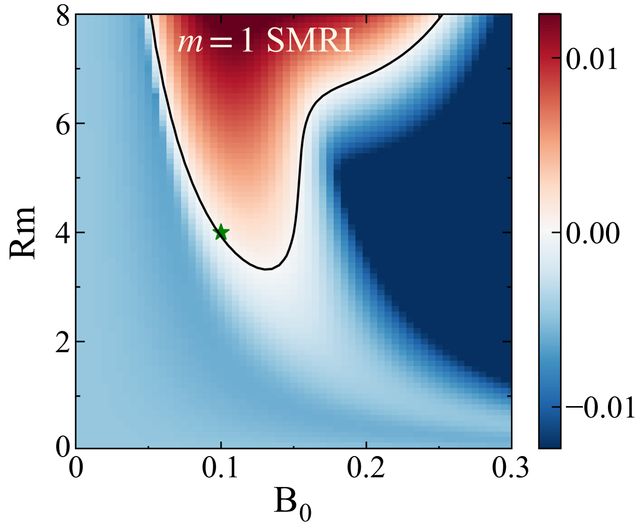

FIG. 2. Criterion for nonaxisymmetric SMRI: normalized growth rate ω_i/Ω_1 of the $(m = 1, n = \pm 2)$ modes calculated by linear analysis with insulating radial BCs in the $\mathrm{Rm} - B_0$ plane. The black curve encloses the unstable region ($m = 1$ SMRI). The green star indicates the case of eigenfunction comparisons between linear analysis and $2D + 1$ simulation shown in Fig. 3.

in z with a wavelength $\lambda_z = 2H/n$, n being an even number, and a base flow with angular velocity depending on radius only, $\Omega(r)$. Here $\omega = \omega_r + i\omega_i$, with ω_r and ω_i being the eigenmode's real angular frequency and growth rate. Other details of the linear analysis are given in Supplemental Material [47].

As depicted in the color plot in Fig. 1, an SSL forms at the joints of the end cap rings after the imposition of the magnetic field, appearing as a local maximum in $q(r)$. This corresponds to a local minimum in the flow's vorticity, $\xi(r) = (2 - q)\Omega$. In our linear analysis, the base flow $\Omega(r)$ is vertically averaged between the two dashed lines to avoid hydrodynamic instabilities (Fig. S1 in Supplemental Material [47]). As shown in Fig. 2, in such a hydrodynamically stable base flow, the $(m, n) = (1, \pm 2)$ modes become unstable for $\mathrm{Rm} \gtrsim 3.5$ and $0.05 \lesssim B_0 \lesssim 0.3$, confirming that it is the $m = 1$ SMRI. Near the onset, the real part ω_r of the unstable $m = 1$ mode's frequency coincides with $\Omega(r)$ at the SSL [the location of the local maximum in $q(r)$], implying the $m = 1$ SMRI originates from the latter. Notably, although the mode remains stable ($\omega_i < 0$) at $\mathrm{Rm} < 3.5$, a moderate magnetic field leads to an enhanced ω_i that persists in the small-Rm limit. This indicates the presence of an inductionless [55] branch of the SSL-induced $m = 1$ SMRI, which scales with the Hartmann number Ha instead of B_0 [Fig. S2(b) in Supplemental Material [47]]. Details will be reported in a future publication. For the same base flow, the (0,2) mode ($m = 0$ SMRI) requires $\mathrm{Rm} \gtrsim 3$ and $0.05 \lesssim B_0 \lesssim 0.3$, a parameter space very close to the $m = 1$ SMRI [Fig. S2(a) in Supplemental Material [47]]. SMRI modes with $m \geq 2$ are stable for $\mathrm{Rm} \leq 100$, making them difficult to excite in any existing experiments. Also, the $n = 2$ mode is the most unstable among all n values All results do not differ significantly for insulating and conducting radial BCs. In contrast, no local extrema exist in the $q(r)$ or $\xi(r)$ of an ideal Couette profile having the same Ω_2/Ω_1 (Fig. S1 in Supplemental Material [47]), and the corresponding $m = 0$ and $m = 1$ SMRI requires $\mathrm{Rm} \gtrsim 10$ and $\mathrm{Rm} \gtrsim 25$, respectively, as shown in Fig. S3 in [47]. Compared to the ideal Couette profile, the reduction in the minimum Rm required for $m = 0$ SMRI is due to the higher q (ratio of shear to rotation) in the SSL [56]. On the other hand, it is most

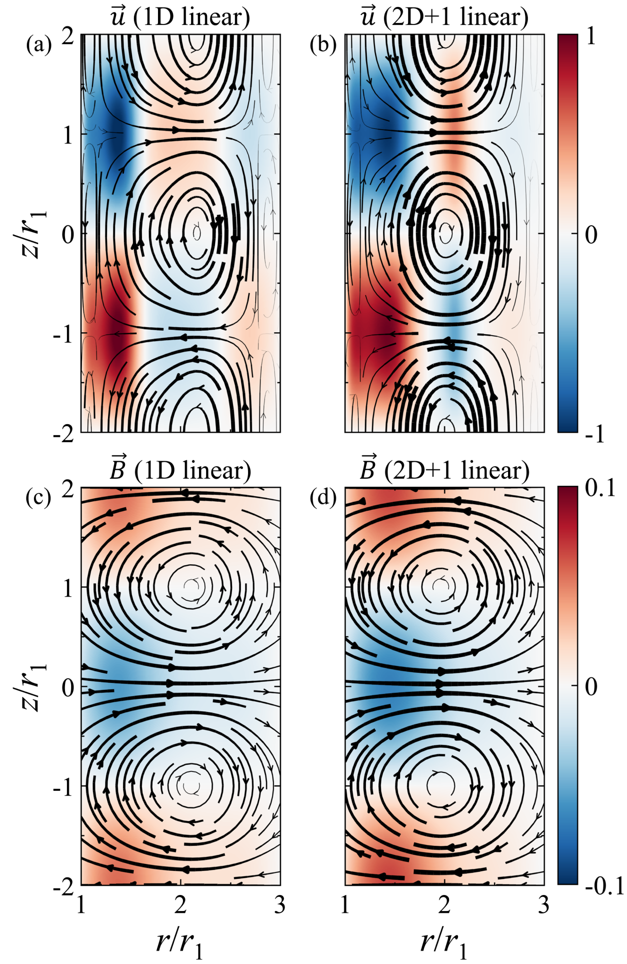

FIG. 3. Global $m = 1$ SMRI structures at $\mathrm{Rm} = 4$ and $B_0 = 0.1$. Poloidal cross-sectional views of eigenfunctions for the superposition of $(m = 1, n = \pm 2)$ modes in velocity field (a) and magnetic field (c) from 1D linear analysis. (b),(d) Corresponding projections of the full $\vec{u}$ and $\vec{B}$ perturbations on $(m = 1, n = \pm 2)$ modes from $2D + 1$ linear simulation with realistic boundary conditions. Curves with arrows represent the poloidal streamlines or field lines constructed from the radial and axial components, and the linewidth is proportional to the local strength of the in-plane velocity and magnetic fields. Color plots show the azimuthal component.

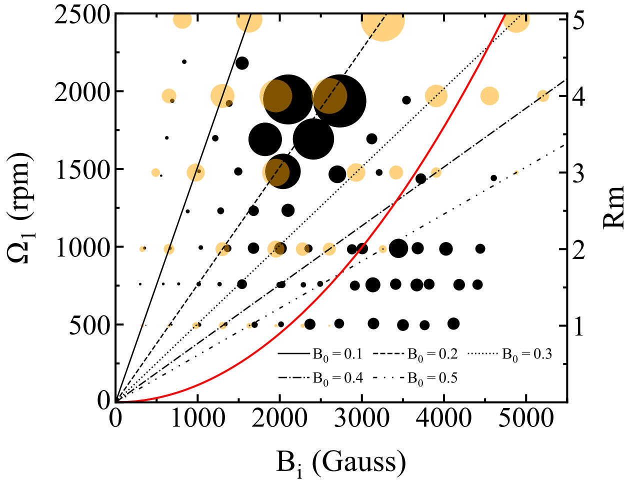

FIG. 4. Bubble plot of the amplitude of the saturated nonaxisymmetric B_r from experiments (black) and 3D simulations (orange). The bubble size is proportional to the amplitude. Straight lines show constant Lehnert number B_0. The red curve represents Elsässer number $\Lambda = 1$. The experimental data were adopted from Ref. [26]. The simulation data are the volume average of the $(m = 1, n = \pm 2)$ modes in B_r.

likely that the reduction in Rm for $m = 1$ SMRI is caused by the local minimum in the base flow's vorticity, since no substantial reduction of Rm is found in an ideal Couette base flow having a larger q. The 1D linear analysis assumes periodicity in z, unlike the simulations and the experiment itself. Nonetheless, as shown by Fig. 3, the superposition of the marginally unstable $(1, \pm 2)$ eigenfunctions from 1D linear analysis (green star in Fig. 2) agrees remarkably well with those from the $2D + 1$ simulation using a two-dimensional base flow and physical end caps. This confirms that the $m = 1$ SMRI exists in an actual device, in which the axial boundaries impose a reflection symmetry about the midplane that leads to its standing-wave structure. Three-dimensional simulations further reveal that this structure persists in the saturated MHD state and becomes dominant over other nonaxisymmetric modes and comparable to the axisymmetric SMRI.

Experimentally, after the imposition of the axial magnetic field B_i, a linear nonaxisymmetric MHD instability with a dominant $m = 1$ structure has recently been observed in the measured B_r at the midplane [26]. As shown in Fig. 4, this instability's amplitude has similar Rm and B_0 dependencies as the $(m = 1, n = \pm 2)$ modes from 3D simulations: both become prominent at Rm $\gtrsim 3$ and $0.1 \lesssim B_0 \lesssim 0.3$. In our system, the SSL becomes hydrodynamically unstable with $n = 0$ once the Elsässer number $\Lambda = B_i^2/\mu_0\rho\eta(\Omega_3 - \Omega_2) > 1$ (red curve) [38]. The prominent bubbles have $\Lambda < 1$, suggesting they are not SSL instability [26]. As such, the consistency between the experiment and the 3D simulation confirms that the observed MHD instability is the nonaxisymmetric SMRI, as predicted by the linear analysis.

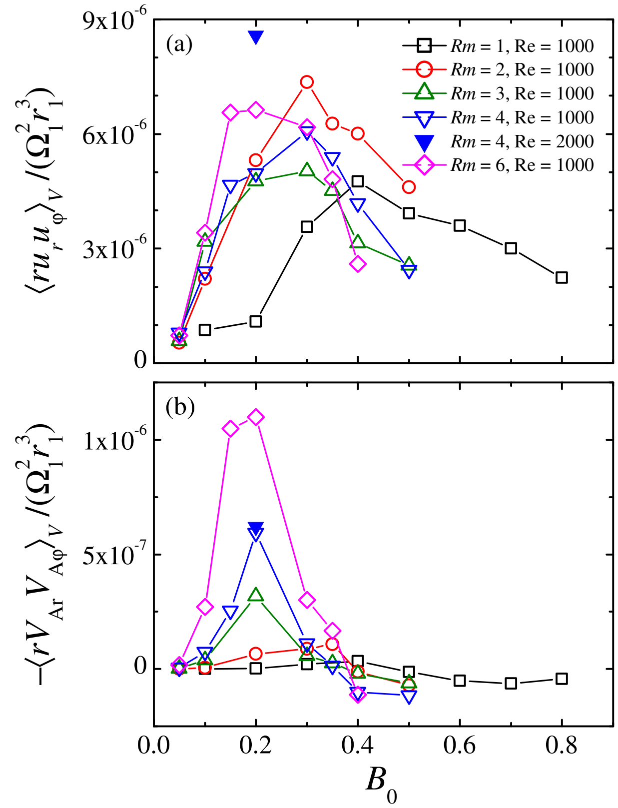

FIG. 5. Calculated Reynolds stress (a) and Maxwell stress (b) contributed by the $(m = 1, n = \pm 2)$ mode, as a function of B_0 at various Rm from 3D simulations. Their sum is the radial angular momentum flux via Eq. (1). The data in both panels are time and volume averages in the saturated MHD state.

The $m = 1$ SMRI induces a radial angular momentum flux via correlations between the radial and azimuthal components of velocity or magnetic fields—i.e., Reynolds or Maxwell stresses. Its normalized form is [5]

$$F_r = \frac{\langle r u_r u_\varphi \rangle_V}{\Omega_1^2 r_1^3} - \frac{\langle r V_{Ar} V_{A\varphi} \rangle_V}{\Omega_1^2 r_1^3}, \tag{1}$$

in which $\langle \ldots \rangle_V$ represents averaging over the entire fluid, and $V_{Ar} = B_r/\sqrt{\mu_0 \rho}$ and $V_{A\varphi} = B_\varphi/\sqrt{\mu_0 \rho}$ represent the Alfvén velocity in the radial and azimuthal directions. The saturated $(1, \pm 2)$ components of velocity and magnetic fields are used to calculate F_r in Eq. (1). Figure 5(a) shows that, for all Rm studied, the Reynolds stress is always positive, first increasing and then decreasing with an increase of B_0. This reveals that the $m = 1$ SMRI prompts an outward angular momentum flux in the velocity field, as for the axisymmetric SMRI. Unlike the amplitude of B_r [see Fig. 5(a)], the Reynolds stress does not increase significantly with increasing Rm beyond Rm ≈ 2. This is likely due to the fixed Re $= 1000$ for most cases studied here, as a case at Re $= 2000$ (solid blue triangle) shows a larger saturated amplitude. The enhancement of the

Reynolds stress (compared to $\mathrm{Rm} \lesssim 1$) occurs over a broader range than that of B_r; this might be caused by residual secondary flows such as Ekman-Hartmann circulation [51,57]. Similarly, as shown in Fig. 5(b), the $(1, \pm 2)$ modes in the magnetic field give rise to an outward angular momentum flux in the $m = 1$ SMRI unstable regime at $\mathrm{Rm} \gtrsim 3$ and $0.1 \lesssim B_0 \lesssim 0.3$. Unlike the Reynolds stress, the Maxwell stress varies with Rm and B_0 in much the same way as B_r amplitude (Fig. 5) and is more consistent with the growth rate shown in Fig. 2. This suggests that the magnetic field is a better diagnostic than the velocities because SMRI is an MHD instability, whereas the velocity can be confounded by hydrodynamic effects.

It has been reported that $m = 1$ SMRI is observed in spherical Taylor-Couette experiments using liquid sodium, where the outer sphere is stationary and the inner sphere is rotating [58]. Although a free-shear layer is present in those experiments, a stationary outer sphere leads to hydrodynamically unstable base flows that introduce other flow modes and even turbulence, complicating the measurements [59]. In particular, the frequency of the free-shear layer in the spherical system is significantly higher than that of the nonaxisymmetric mode, meaning that the latter is unlikely to be excited via the nonaxisymmetric SMRI mechanism discussed here.

To summarize, we have presented the first confirmation of nonaxisymmetric SMRI with $m = 1$ azimuthal structure in liquid-metal Taylor-Couette flow using combined theoretical, numerical, and experimental methods. Linear theory predicts that the $m = 1$ SMRI can be introduced at $\mathrm{Rm} \gtrsim 3$ via a free-shear layer in a hydrodynamically stable base flow, which gives rise to a local minimum in the vorticity profile. Numerical simulations confirm the theoretical results in an actual device with vertical end caps and further reveal that the $m = 1$ SMRI has a standing-wave structure in the poloidal cross section, introducing a prominent radial magnetic field in the midplane. It also reveals that the $m = 1$ SMRI introduces an outward angular momentum flux in both velocity and magnetic fields, just like the axisymmetric SMRI. By obtaining a good agreement between experiments and simulations for the Rm and B_0 dependence of the amplitude of the nonaxisymmetric radial magnetic field, the existence of $m = 1$ SMRI is thus confirmed. To further understand the essential physics underlying the SSL-induced SMRI, it is beneficial to develop a unifying theoretical framework applicable to different base flows. Its relationship with curvature effects [60,61] and magnetized Rossby wave instabilities [62] with nonzero n needs elucidation. Comparisons of its frequency and growth rates between the two linear methods will be conducted. Vertical Hall probe arrays will be used in the experiment to reveal the $n = 2$ nature of the $m = 1$ SMRI. Simulations using the entropy-viscosity method will achieve Re closer to experiments [63].

Acknowledgments—The authors thank Professor Jean-Luc Guermond and Professor Caroline Nore for their permission and assistance in using the SFEMaNS code. This research was supported by U.S. DOE (Contract No. DE-AC02-09CH11466), NASA (Grant No. NNH15AB25I), NSF (Grant No. AST-2108871), and the Max-Planck-Princeton Center for Plasma Physics (MPPC). E. G. and H. J. acknowledge support by S. Prager and Princeton University.

Data availability—Digital data associated with this work are available from the Princeton Data Commons at Princeton University [64].

[1] J. Frank, A. King, and D. J. Raine, *Accretion Power in Astrophysics* (Cambridge University Press, Cambridge, England, 2002).

[2] E. P. Velikhov, Stability of an ideally conducting liquid flowing between cylinders rotating in a magnetic field, Sov. Phys. JETP **36**, 995 (1959).

[3] S. Chandrasekhar, The stability of non-dissipative Couette flow in hydromagnetics, Proc. Natl. Acad. Sci. U.S.A. **46**, 253 (1960).

[4] S. A. Balbus and J. F. Hawley, A powerful local shear instability in weakly magnetized disks, Astrophys. J. **376**, 214 (1991).

[5] S. A. Balbus and J. F. Hawley, Instability, turbulence, and enhanced transport in accretion disks, Rev. Mod. Phys. **70**, 1 (1998).

[6] K. Akiyama *et al.* (Event Horizon Telescope Collaboration), First M87 event horizon telescope results. VIII. Magnetic field structure near The event horizon, Astrophys. J. Lett. **910**, L13 (2021).

[7] G. Rüdiger and R. Hollerbach, New type of magnetorotational instability in cylindrical Taylor-Couette flow, Phys. Rev. Lett. **95**, 124501 (2005).

[8] F. Stefani, T. Gundrum, G. Gerbeth, G. Rüdiger, M. Schultz, J. Szklarski, and R. Hollerbach, Experimental evidence for magnetorotational instability in a Taylor-Couette flow under the influence of a helical magnetic field, Phys. Rev. Lett. **97**, 184502 (2006).

[9] R. Hollerbach, V. Teeluck, and G. Rüdiger, Nonaxisymmetric magnetorotational instabilities in cylindrical Taylor-Couette flow, Phys. Rev. Lett. **104**, 044502 (2010).

[10] M. Seilmayer, V. Galindo, G. Gerbeth, T. Gundrum, F. Stefani, M. Gellert, G. Rüdiger, M. Schultz, and R. Hollerbach, Experimental evidence for nonaxisymmetric magnetorotational instability in a rotating liquid metal exposed to an azimuthal magnetic field, Phys. Rev. Lett. **113**, 024505 (2014).

[11] W. Liu, J. Goodman, I. Herron, and H. Ji, Helical magnetorotational instability in magnetized Taylor-Couette flow, Phys. Rev. E **74**, 056302 (2006).

[12] O. N. Kirillov, F. Stefani, and Y. Fukumoto, A unifying picture of helical and azimuthal MRI, and the universal significance of the Liu limit, Astrophys. J. **756**, 83 (2012).

[13] K. Akiyama *et al.* (Event Horizon Telescope Collaboration), First M87 Event Horizon Telescope results. I. The shadow

of the supermassive black hole, Astrophys. J. Lett. **875**, L1 (2019).
[14] K. Akiyama *et al.* (Event Horizon Telescope Collaboration), First Sagittarius A* Event Horizon Telescope results. I. The shadow of the supermassive black hole in the center of the Milky Way, Astrophys. J. Lett. **930**, L12 (2022).
[15] L. Rayleigh, On the dynamics of revolving fluids, Proc. R. Soc. A **93**, 148 (1917).
[16] H. Ji, M. Burin, E. Schartman, and J. Goodman, Hydrodynamic turbulence cannot transport angular momentum effectively in astrophysical disks, Nature (London) **444**, 343 (2006).
[17] Y. Wang, E. P. Gilson, F. Ebrahimi, J. Goodman, and H. Ji, Observation of axisymmetric standard magnetorotational instability in the laboratory, Phys. Rev. Lett. **125**, 115001 (2022).
[18] A. Brandenburg, A. Nordlund, R. F. Stein, and U. Torkelsson, Dynamo-generated turbulence and large-scale magnetic fields in a Keplerian shear flow, Astrophys. J. **446**, 741 (1995).
[19] J. F. Hawley, C. F. Gammie, and S. A. Balbus, Local three-dimensional simulations of an accretion disk hydromagnetic dynamo, Astrophys. J. **464**, 690 (1996).
[20] F. Rincon, G. I. Ogilvie, and M. R. E. Proctor, Self-sustaining nonlinear dynamo process in Keplerian shear flows, Phys. Rev. Lett. **98**, 254502 (2007).
[21] G. Lesur and G. I. Ogilvie, On self-sustained dynamo cycles in accretion discs, Astron. Astrophys. **488**, 451 (2008).
[22] F. Ebrahimi and E. G. Blackman, Radially dependent large-scale dynamos in global cylindrical shear flows and the local Cartesian limit, Mon. Not. R. Astron. Soc. **459**, 1422 (2016).
[23] P. Bhat, F. Ebrahimi, and E. G. Blackman, Large-scale dynamo action precedes turbulence in shearing box simulations of the magnetorotational instability, Mon. Not. R. Astron. Soc. **462**, 818 (2016).
[24] A. Riols, H. Latter, and E. G. Blackman, Magnetorotational instability and dynamo action in gravito-turbulent astrophysical discs, Mon. Not. R. Astron. Soc. **474**, 2212 (2017).
[25] L. E. Held and G. Mamatsashvili, MRI turbulence in accretion discs at large magnetic Prandtl numbers, Mon. Not. R. Astron. Soc. **517**, 2309 (2022).
[26] Y. Wang, E. P. Gilson, F. Ebrahimi, J. Goodman, K. J. Caspary, H. W. Winarto, and H. Ji, Identification of a non-axisymmetric mode in laboratory experiments searching for standard magnetorotational instability, Nat. Commun. **13**, 4679 (2022).
[27] G. Rüdiger and M. Schultz, The gap-size influence on the excitation of magnetorotational instability in cylindric Taylor-Couette flows, J. Plasma Phys. **90**, 905900105 (2024).
[28] F. Stefani, A. Gailitis, G. Gerbeth, A. Giesecke, Th. Gundrum, G. Rüdiger, M. Seilmayer, and T. Vogt, The DRESDYN project: Liquid metal experiments on dynamo action and magnetorotational instability, Geophys. Astrophys. Fluid Dyn. **113**, 51 (2019).
[29] A. Mishra, G. Mamatsashvili, and F. Stefani, From helical to standard magnetorotational instability: Predictions for upcoming liquid sodium experiments, Phys. Rev. Fluids **7**, 064802 (2022).
[30] A. Mishra, G. Mamatsashvili, and F. Stefani, Nonlinear evolution of magnetorotational instability in a magnetized Taylor-Couette flow: Scaling properties and relation to upcoming DRESDYN-MRI experiment, Phys. Rev. Fluids **8**, 083902 (2023).
[31] A. Mishra, G. Mamatsashvili, and F. Stefani, Nonaxisymmetric modes of magnetorotational and possible hydrodynamical instabilities in the upcoming DRESDYN-MRI experiments: Linear and nonlinear dynamics, Phys. Rev. Fluids **9**, 033904 (2024).
[32] F. Stefani, Liquid-metal experiments on geophysical and astrophysical phenomena, Nat. Rev. Phys. **6**, 409 (2024).
[33] J. Shercliff, Steady motion of conducting fluids in pipes under transverse magnetic fields, Math. Proc. Cambridge Philos. Soc. **49**, 136 (1953).
[34] B. Lehnert, An instability of laminar flow of mercury caused by an external magnetic field, Proc. R. Soc. A **233**, 299 (1955).
[35] K. Stewartson, On almost rigid rotations, J. Fluid Mech. **3**, 17 (1957).
[36] E. J. Spence, A. H. Roach, E. M. Edlund, P. Sloboda, and H. Ji, Free magnetohydrodynamic shear layers in the presence of rotation and magnetic field, Phys. Plasmas **19**, 056502 (2012).
[37] C. Gissinger, J. Goodman, and H. Ji, The role of boundaries on the magnetorotational instabilities, Phys. Fluids **24**, 074109 (2012).
[38] A. H. Roach, E. J. Spence, C. Gissinger, E. M. Edlund, P. Sloboda, J. Goodman, and H. Ji, Observation of a free-Shercliff-layer instability in cylindrical geometry, Phys. Rev. Lett. **108**, 154502 (2012).
[39] A. H. Roach, Velocity measurements and free-shear-layer instabilities in a rotating liquid metal, Ph.D thesis, Princeton University, 2013.
[40] J. E. Pringle, Soft x-ray emission from dwarf novae, Mon. Not. R. Astron. Soc. **178**, 195 (1977).
[41] M. A. Belyaev and E. Quataert, Inefficient angular momentum transport in accretion disc boundary layers, Mon. Not. R. Astron. Soc. **479**, 1528 (2018).
[42] W. R. Ward and K. Hourigan, Orbital migration of protoplanets: The inertial limit, Astrophysics. J. **347**, 490 (1989).
[43] J. C. B. Papalouzou and C. Terquem, Planet formation and migration, Rep. Prog. Phys. **69**, 119 (2006).
[44] J. Schumacher and E. R. Sreenivasan, Colloquium: Unusual dynamics of convection in the Sun, Mon. Not. R. Astron. Soc. **92**, 041001 (2020).
[45] G. M. Vasil, D. Lecoanet, K. Augustson, K. J. Burns, J. S. Oishi, B. P. Brown, N. Brummell, and K. Julien, The solar dynamo begins near the surface, Nature (London) **629**, 769 (2024).
[46] H. Klahr and A. Hubbard, Convective overstability in radially stratified accretion disks under thermal relaxation, Astrophys. J. **788**, 21 (2014).
[47] See Supplemental Material at http://link.aps.org/supplemental/10.1103/PhysRevLett.134.135101 for additional results and a detailed discussion of the global linear analysis, which includes Refs. [48,49].
[48] J. Goodman and H. Ji, Magnetorotational instability of dissipative Couette flow, J. Fluid Mech. **462**, 365 (2002).
[49] G. Rüdiger, M. Schultz, and D. Shalybkov, Linear magneto-hydrodynamic Taylor-Couette instability for liquid sodium, Phys. Rev. E **67**, 046312 (2003).

[50] H. W. Winarto, H. Ji, J. Goodman, F. Ebrahimi, E. P. Gilson, and Y. Wang, Parameter space mapping of the Princeton magnetorotational instability experiment, Phys. Rev. E **102**, 023113 (2020).

[51] X. Wei, H. Ji, J. Goodman, F. Ebrahimi, E. Gilson, F. Jenko, and K. Lackner, Numerical simulations of the Princeton magnetorotational instability experiment with conducting axial boundaries, Phys. Rev. E **94**, 063107 (2016).

[52] E. M. Edlund and H. Ji, Nonlinear stability of laboratory quasi-Keplerian flows, Phys. Rev. E **89**, 021004(R) (2014).

[53] J. L. Guermond, R. Laguerre, J. Léorat, and C. Nore, Nonlinear magnetohydrodynamics in axisymmetric heterogeneous domains using a Fourier/finite element technique and an interior penalty method, J. Comput. Phys. **228**, 2739 (2009).

[54] K. J, Burns, G. M. Vasil, J. S. Oishi, D. Lecoanet, and B. P. Brown, DEDALUS: A flexible framework for numerical simulations with spectral methods, Phys. Rev. Res. **2**, 023068 (2020).

[55] H. Ji and J. Goodman, Taylor-Couette flow for astrophysical purposes, Phil. Trans. R. Soc. A **381**, 20220119 (2023).

[56] H. Ji, J. Goodman, and A. Kageyama, Magnetorotational instability in a rotating liquid metal annulus, Mon. Not. R. Astron. Soc. **325**, L1 (2001).

[57] J. Szklarski and G. Rüdiger, Ekman-Hartmann layer in a magnetohydrodynamic Taylor-Couette flow, Phys. Rev. E **76**, 066308 (2007).

[58] D. Sisan, N. Mujica, W. Tillotson, Y. Huang, W. Dorland, A. Hassam, T. Antonsen, and D. Lathrop, Experimental observation and characterization of the magnetorotational instability, Phys. Rev. Lett. **93**, 114502 (2004).

[59] C. Gissinger, H. Ji, and J. Goodman, Instabilities in magnetized spherical Couette flow, Phys. Rev. E **84**, 026308 (2011).

[60] F. Ebrahimi and M. Pharr, A nonlocal magneto-curvature instability in a differentially rotating disk, Astrophys. J. **936**, 145 (2022).

[61] F. Ebrahimi and A. Haywood, A generalized effective potential for differentially rotating plasmas, Phys. Plasmas **32**, 030702 (2025).

[62] C. Cui, A. Tripathi, C. Yu, M. Lin, and A, Youdin, Rossby wave instability in weakly ionized protoplanetary discs-I. Azimuthal or vertical B-fields, Mon. Not. R. Astron. Soc. **537**, 1973 (2025).

[63] J. L. Guermond, R. Pasquetti, and B. Popov, From suitable weak solutions to entropy viscosity, J. Sci. Comput. **49**, 35 (2011).

[64] Yin Wang, Princeton Data Commons (2025), 10.34770/38k9-rm86.